JOURNAL OF COMPUTATIONAL PHYSICS 34, 287–313 (1980)

Separating Flow Near a Static Contact Line: Slip at a Wall and Shape of a Free Surface

WILLIAM J. SILLIMAN AND L. E. SCRIVEN

Department of Chemical Engineering and Materials Science, University of Minnesota, Minneapolis, Minnesota 55455

Received January 10, 1979; revised April 4, 1979

The effects of replacing the usual no-slip boundary condition by a slip-coefficient boundary condition on solid walls are determined by means of Galerkin finite element solutions of the Navier–Stokes equation system for steady two-dimensional discharge of liquid from a sharp-edged slot—the "die-swell" flow, in which menisci separate from contact lines on the die edges. A velocity pressure formulation is used with a mixed interpolation basis of quadratic serendipity elements for velocity and bilinear functions for pressure. Alternate formulations of the free meniscus computation are examined; iteration on the normal stress condition proves superior except when surface tension is low. Even if slip is possible, the no-slip boundary condition proves accurate for Newtonian die-swell flow, provided the slip coefficient β is less than $10^{-3}\, b/\mu$ (μ, viscosity; b, the channel half-width). Slip at the solid wall alleviates the apparent stress singularity at the exit. When $\beta \geqslant 10^{-3}\, b/\mu$, slip reduces die swell even of Newtonian liquid; local slip near the contact line is sufficient. Raising the Reynolds number decreases the upstream influence at the exit on the velocity profile and reduces die swell. Surface tension straightens the free meniscus profile and thus reduces die swell. Profile straightening is compounded by actions of surface tension and slip together.

1. INTRODUCTION

The physics of flow in the vicinity of a contact line where a fluid interface separates from a solid surface is not clear. The subject is under investigation from both molecular (Salter [1]; Del Cerro and Jameson [2]; Salter *et al.* [3]) and continuum viewpoints (Huh [4]; Huh and Scriven [5]; Richardson [6]; Michael [7]; Hocking [8]; Dussan [9]; Huh & Mason [10]; Silliman and Scriven [11]). At the continuum level there is no difficulty when the contact line is straight and static and flow in its neighborhood is rectilinear and parallel to it. Indeed, analysis of rectilinear rivulet flow on inclined surfaces is straightforward (Towell and Rothfeld [12]; Kern [13]; Bentwich *et al.* [14]). However, when there is flow perpendicular to the contact line, i.e., at a separation line, conventional fluid mechanical analysis indicates that exceedingly high stresses should occur in the neighborhood of the line. These include wall shear stress large enough to raise the question of whether liquid can after all slip along a solid boundary. If so, then the "no-slip" boundary condition of fluid mechanics may

0021-9991/80/030287–27$02.00/0

not be adequate in the neighborhood of a contact line. While Navier [15] formulated a boundary condition of the third kind which admits slip, Stokes [16] argued for the more specialized boundary condition of the first kind, which does not. The controversy they launched was settled by experiments with flow past fully wetted surfaces, the ultimate experiments of that era being those of Whetham [17] with capillary tubes. The no-slip hypothesis was universally adopted for liquid flow past solid on the basis of experimental evidence obtained in the absence of contact lines. Thus the question of slip near contact lines remains open.

Reasons for questioning the no-slip hypothesis are the *infinite* stresses at contact, or separation, lines predicted by theoretical analyses by Richardson [6] and Michael [7]. Such stresses are also indicated by the finite-element simulation by Nickell *et al.* [18]. As Huh and Scriven [5] pointed out, there is from the standpoint of continuum physics a need of relief from stress singularites at contact lines, for Nature abhors infinities. The occurrence of an infinity in continuum physics signals breakdown of one or more premises of the theory. Possible reliefs from the stress singularities at moving contact lines, where the singularity is nonintegrable, were discussed by Huh and Scriven [5] and investigated further by Hocking [8, 19], Dussan and Davis [20], Dussan [9], and Huh and Mason [10]. The singularity at a static contact line evidently is integrable, e.g., the total shear force on the solid wall upstream is finite. But though this singularity is weaker than that at a moving contact line, it has so far received less attention in the literature.

Apparent slip on the macroscopic hydrodynamic scale may originate in any of several different phenomena at smaller-length scales [21]. As Hocking [8] pointed out, on the microscopic hydrodynamic scale of the amplitude of surface roughness, liquid—though it did not slip locally past the solid surface—could appear to slip at a mathematical surface located at the mean elevation of the rugosities of the solid. This appearance could be accentuated by the presence of lower viscosity gas in the pits and grooves of the rough solid surface [8]. Similarly, as in certain flowing polymeric liquids where viscosity and even composition are highly dependent on shear rate and shear stress, apparent slip could arise in a thin stratum of liquid of lower viscosity formed next to all of a smooth solid surface [22] or preferentially in regions of higher shear next to the peaks and ridges of a rough solid. This is one way a different constitutive behavior of the liquid adjacent to the solid surface could arise, particularly in areas of high shear. On the scale of long-range force interactions between liquid and solid, i.e., the normally submicron scale of electrical double-layer and quantum mechanical Van der Waals or dispersion forces, the constitutive behavior of the liquid might be altered to reduce effective viscosity (however, indications are that effective viscosity next to a solid is likely higher, not lower: cf. [23, 24]). Such an effect also could vary locally according to the topography of the solid. Finally, on the molecular scale there might be "true" slip, i.e., appreciable departure locally from the thermodynamic equilibrium distribution of molecular velocities within a small number of molecular diameters' distance from the solid such that molecules of one layer shift past those of another in some degree of coordinated, directed motion (as in slip in rarefied gas dynamics: cf. [25]). The ultimate slip on this scale would be outright

shear fracture, as within a solid or between bonded solids—cohesive or adhesive failure, respectively.

On the macroscopic hydrodynamic scale it appears that any of these mechanisms can be modeled, crudely at least, by extrapolating the macroscopic constitutive behavior, including the viscosity coefficient, to a suitably located smooth mathematical surface to represent the liquid–solid boundary region, and assigning there a transfer coefficient for tangential momentum which multiplies the discontinuity between extrapolated tangential velocity of the fluid, $\mathbf{u}$, and the tangential velocity of the solid, $\mathbf{u}_S$. The product is the flux of tangential momentum across the mathematical surface. This flux must equal that transmitted to the surface by the action of viscosity in the liquid. Thus, if $\mathbf{T}$ is the stress tensor in the liquid, $\mathbf{n}$ the unit normal to the surface, and $\mathbf{1}_{II} \equiv \mathbf{1} - \mathbf{nn}$ the geometric tensor that projects vectors onto the local tangent plane to the surface, one has

$$-(1/\beta)\,\mathbf{1}_{II} \cdot (\mathbf{u} - \mathbf{u}_S) = \mathbf{1}_{II} \cdot (\mathbf{n} \cdot \mathbf{T}). \tag{1.1}$$

This is Navier's [15] slip condition at a solid wall, in full vector form. The momentum transfer coefficient is written as $1/\beta$, where β is the slip coefficient. Both are positive quantities and a minus sign appears in (1.1) because momentum must be transferred across the velocity discontinuity from faster-moving to slower-moving fluid, just as shear viscosity must be positive in the Newtonian constitutive relation for continuous velocity fields, in order to account for tangential momentum transfer down a velocity gradient. In two-dimensional flow configurations the projection tensor is given simply by $\mathbf{1}_{II} = \mathbf{tt}$, where $\mathbf{t}$ is the unit tangent to the surface, and Navier's slip condition becomes [11]

$$-(1/\beta)\,\mathbf{t} \cdot (\mathbf{u} - \mathbf{u}_S) = \mathbf{nt} : \mathbf{T}. \tag{1.2}$$

Equations (1.1) and (1.2) relate velocity and velocity gradients at the boundary and are thus boundary conditions of the third kind. β may depend on the stress tensor $\mathbf{T}$ and otherwise on location along the boundary surface. If it is independent of the stress tensor and the stress tensor is that for Newtonian fluid, (1.1) and (1.2) are linear boundary conditions. The limit $\beta \to \infty$ gives perfect slip, i.e., $\mathbf{n} \cdot \mathbf{T} \cdot \mathbf{1}_{II} = \mathbf{0}$. The limit $\beta \to 0$ gives no slip, i.e., $\mathbf{u} = \mathbf{u}_S$.

In this paper we analyze the two-dimensional, steady flow of incompressible Newtonian liquid out of a sharp-cornered slot, with and without slip along the two, parallel mathematical planes chosen to represent the channel walls upstream of the corners. We contrast the effect of applying (1.2) instead of no slip over the entire wall versus just in the upstream vicinity of the corner. We suppose that the flow separates from the solid walls at the sharp corners, as in Fig. 1, which shows the well-known die-swell case. Thus the corners are three-phase contact lines at which the two free menisci of the liquid jet are pinned to the solid walls. We compare the solutions without and with slip for two purposes: first, for indications that absence of slip generates infinite stress at the contact lines and presence of slip alleviates the stress singularity; and second, to see to what extent the solutions with no slip can be used in place of those with the slip allowed by Navier's old hypothesis.

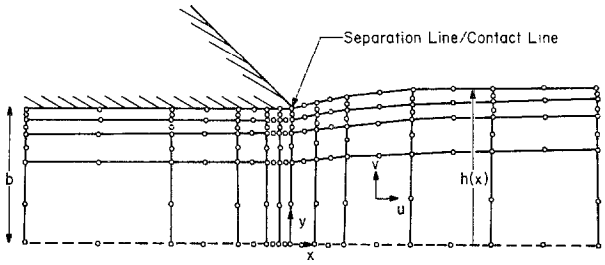

FIG. 1. Die-swell geometry and mesh employed in comparisons of numerical solutions.

In either case the flow domain is irregular and the problem is intractable by convential mathematical analysis employing an infinite set of basis functions defined on a standard domain. Instead we use a finite set of basis functions each defined on a subdomain of adjustable size and shape and, though we lose higher-order differentiability which would actually be superfluous, we arrive at an approximate solution which is accurate in a weighted-residual sense. In particular we use the Galerkin finite element method based on the divergence form of the Navier–Stokes and continuity equations [26], with a mixed interpolation consisting of quadratic serendipity elements for Cartesian velocity components and bilinear elements for pressure [27]. The free meniscus is curved and for the subdomains adjoining it we use curvilinear rectangles each having one side that approximates a portion of meniscus. The thicknesses of successive ranks of subdomains are in constant ratios to the distance between the free meniscus and the symmetry plane; the menisci themselves are interpolated with quadratic isoparametric elements for flow field calculations, and with Hermite cubic or arc-of-circle elements for curvature estimates. In the neighborhood of the slot exit the velocity and pressure gradients are relatively steep and so there we choose smaller subdomains. The finite element mesh for most of the work is shown in Fig. 1; results were checked by repeating calculations with refined meshes in the neighborhood of the contact line or, in certain cases, with full quadratic (nine-point) elements. For meniscus problems with regions of steep gradients the finite element method, though it is more laborious to program for automatic calculations, has distinct advantages over finite difference approximations [18].

The solutions depend on computation of the meniscus profiles. Previously this has been done in the finite element method by means of Picard iteration techniques [18, 28] that proceed in a three-part cycle: (i) a meniscus shape is assigned; (ii) a flow field within that shape is calculated after temporarily discarding *one* of the *three* boundary conditions at the meniscus, viz., the kinematic condition, the normal stress balance, or the vanishing of shear stress (unless one of these is relaxed the flow problem is overspecified); and (ii) a new meniscus shape is then computed to satisfy as closely as possible the boundary condition that was temporarily relaxed, and the cycle is repeated until the desired degree of convergence is attained—if it does indeed converge. The best choice of boundary condition to relax was not known and has been the subject of controversy.

In this paper we investigate two leading alternatives, employing as an aid a closely related successive approximation procedure for systems of linear equations. The behavior of the linear problem provides insights which we find are confirmed by the results of computing solutions of the full nonlinear problem for a wide range of capillary:

2. Basic Formulation

The weak form of the Navier-Stokes and continuity equations for two-dimensional, steady, incompressible flow is well established and the finite element version is easily constructed once the basis functions are chosen for expanding the component velocities (here taken to be Cartesian components), the pressure, and the location of the meniscus:

$$u = \sum_{i=1}^{N} u_i \phi^i(x, y), \quad v = \sum_{i=1}^{N} v_i \phi^i(x, y), \quad p = \sum_{i=1}^{M} p_i \psi^i(x, y), \quad h = \sum_{i=1}^{S} h_i \chi^i(x). \tag{2.1}$$

Our choices for the ϕ_i's, ψ_i's, and χ_i's are named above; those for the ϕ_i's and ψ_i's are the ones recommended by Gartling *et al.* [27]. With body forces excluded, the momentum equations are

$$\int_A \nabla \phi^i \cdot \mathbf{T}\, dA - \int_{\partial A} \phi^i \mathbf{n} \cdot \mathbf{T}\, ds + N_{\mathrm{Re}} \int_A \phi^i \mathbf{u} \cdot \nabla \mathbf{u}\, dA = \mathbf{0}, \tag{2.2}$$

where $\mathbf{T} = -p\mathbf{1} + [\nabla \mathbf{u} + (\nabla \mathbf{u})^T]$, ∂A is the boundary of the flow domain A, and $N_{\mathrm{Re}} \equiv (vb)^{-1} \int u\, dy$ is of course Reynolds number. On the boundaries the traction $\mathbf{n} \cdot \mathbf{T}$ can be decomposed into normal and tangential parts to give

$$\int_A \nabla \phi^i \cdot \mathbf{T}\, dA - \int_{\partial A} \phi^i (\mathbf{nt} : \mathbf{T})\, \mathbf{t}\, ds - \int_{\partial A} \phi^i (\mathbf{nn} : \mathbf{T})\, \mathbf{n}\, ds + N_{\mathrm{Re}} \int \phi \mathbf{u} \cdot \nabla \mathbf{u}\, dA = \mathbf{0}. \tag{2.3}$$

Each of these momentum equations is to be resolved into x- and y-components. The continuity equations are

$$\int_A \psi^i \nabla \cdot \mathbf{u}\, dA = 0. \tag{2.4}$$

Along each portion of the boundary (Fig. 1) there must be one boundary condition for the x-momentum equations and one for the y-momentum equations. In addition, along the meniscus a third condition is necessary because its location is unknown a priori. With an open system as in Fig. 1, conditions at the inflow and outflow are needed. Asymptotic behavior can easily be deduced: The inlet velocity profiles are rectilinear and semiparabolic $u(x, y) = g(y) \equiv a_0 + a_1 y + a_2 y^2$ (appropriate a_0, a_1, and a_2) and $v(x, y) = 0$; whereas far downstream the outlet velocity profile is flat,

$u(x, y) =$ constant, and $v(x, y) = 0$. At the exit then $\mathbf{nn} : \boldsymbol{\tau} = 0$, where $\boldsymbol{\tau} \equiv \nabla\mathbf{u} + (\nabla\mathbf{u})^T$ is the viscous stress. Calculations are made with the inflow and outflow conditions prescribed at large but *finite* distances from the exit; tests must be performed to ensure that the distances are great enough not to affect results in the domain of interest. The set of conditions is

At inflow plane:	$\mathbf{n} \cdot \mathbf{u} = g(y)$	$\mathbf{t} \cdot \mathbf{u} = 0$	(2.5a, *b*)
At outflow plane:	$\mathbf{nn} : \boldsymbol{\tau} = 0$	$\mathbf{t} \cdot \mathbf{u} = 0$	(2.5c, d)
At midplane of symmetry:	$\mathbf{tn} : \mathbf{T} = 0$	$\mathbf{n} \cdot \mathbf{u} = 0$	(2.5e, f)
At solid walls:	$B\mathbf{tn} : \mathbf{T} + \mathbf{t} \cdot \mathbf{u} = 0$	$\mathbf{n} \cdot \mathbf{u} = 0$	(2.5g, h)
At free meniscus	$\mathbf{tn} : \mathbf{T} = 0$	$N_{\mathrm{Ca}}\mathbf{nn} : \mathbf{T} = 2H - \mathrm{N}_{\mathrm{Ca}}p^*$	(2.5i, j)
		$\mathbf{n} \cdot \mathbf{u} = 0$	(2.5k)

The slip parameter and capillary number are, respectively,

$$B \equiv \beta\mu/b \qquad \text{and} \qquad N_{\mathrm{Ca}} \equiv \mu U/\sigma,$$

where b is the half-breadth of the channel, μ the liquid viscosity, U the average volumetric flow rate per unit area, and σ the surface tension of the free meniscus; the mean curvature of the latter is given by

$$2H = h_{xx}(1 + h_x^2)^{-3/2}, \tag{2.6}$$

where h is distance from the midplane of symmetry and subscript x denotes differentiation with respect to x. p_* is the level of total normal stress on the meniscus where it has zero mean curvature, whether or not such a plane actually exists in the flow domain. In die swell p_* is equal to zero. Specification of p_* can be considered to be a "meniscus equation" boundary condition [29] as can the two other conditions which the meniscus must meet in the die-swell case: $h = 1$ at die exit, and $h_x = 0$ at outflow plane. Finally, pressure is arbitrary up to an additive constant p_0 (which in die swell can be set to the pressure in the exterior fluid): in the continuous case the solution can be expressed in terms of $p - p_0$; however, in the discretized case the corresponding procedure is to set $p_0 = 0$.

The essential boundary conditions are those involving only the velocity, not the stress, and must be satisfied by the basis functions ϕ^i chosen at (2.1). The natural boundary conditions are those involving only the stress and are eventually combined with boundary terms in equations for residuals in the Galerkin procedure. The slip

equation (2.5g) is a boundary condition of the third kind, or Robin condition, and must be incorporated as the term [30]

$$\int \phi^i \frac{1}{B} \mathbf{t} \cdot \mathbf{u} \, ds.$$

Now when expansions (2.1) are substituted in (2.3)–(2.5), the result is a set of simultaneous nonlinear algebraic equations expressing the conditions that the residual of the x-momentum equation and the residual of the y-momentum equations each be orthogonal to all of the ϕ^i's, and that of the continuity equation be orthogonal to all of the ψ^i's. There is a single equation for the free meniscus node at the outflow plane, where the pressure level p_* in the liquid is specified. Also in the set are equations requiring certain boundary residuals to be orthogonal to the χ_i's, or an equivalent equation subset for the h_i's. The unknowns in the algebraic equations are the coefficients u_i, v_i, p_i, and h_i in (2.1), which are nodal values on the finite element mesh (cf. Fig. 1). Suppose there are s velocity nodes on the meniscus (including the one at the contact line and the one at the outflow plane) and b velocity nodes elsewhere on the boundary. The number of meniscus elevation nodes is of course s also. Then $n \equiv N - s - b$ is the number of internal velocity nodes. The total number of pressure nodes is m. The columns of a matrix can be identified with each of these unknowns; a convenient ordering is shown in Fig. 2. The rows of the matrix can be identified with the algebraic equations, which are arranged in a convenient order in Fig. 2. If a given unknown does not appear in a given equation, let the corresponding matrix element be zero; if it does, let the element be the term(s) in the equation in which the unknown occurs. This is the *incidence array* of the equation set (the name applies also to the purely numerical matrix where the nonzero elements are all replaced by unity). Rather than displaying all of the elements, Fig. 2 shows only the fill structure, i.e., those rectangular blocks which contain zeros exclusively and those blocks which do not. The fill structure clarifies the relationships among alternative strategies for solving the equation set [31]. Here the occurrence of identical nonzero elements in different rows of the same column is critical. The reason is that the integration by parts in the Galerkin procedure generates boundary terms that match terms in boundary conditions—boundary conditions that govern fluxes in and out of the flow domain.

What is immediately evident about the incidence array in Fig. 2 is that it is rectangular: there are more equations than unknowns. Indeed, the number of unknowns is $3s + 2(n + b) + m + 1$, whereas the number of equations is $5s + 2(n + b) + m + 1$, an excess of $2s$. However, the momentum and continuity equations do not form an independent set until $2s$ boundary conditions have been combined with them. Plainly, among the total of $3s$ meniscus boundary conditions there are many ways of selecting $2s$.

One alternative is to substitute the s normal stress and s shear stress boundary conditions into the momentum equations and retain the s kinematic boundary conditions as autonomous. A second alternative is to substitute the s shear stress boundary conditions into the momentum equations, use the s kinematic conditions as essential

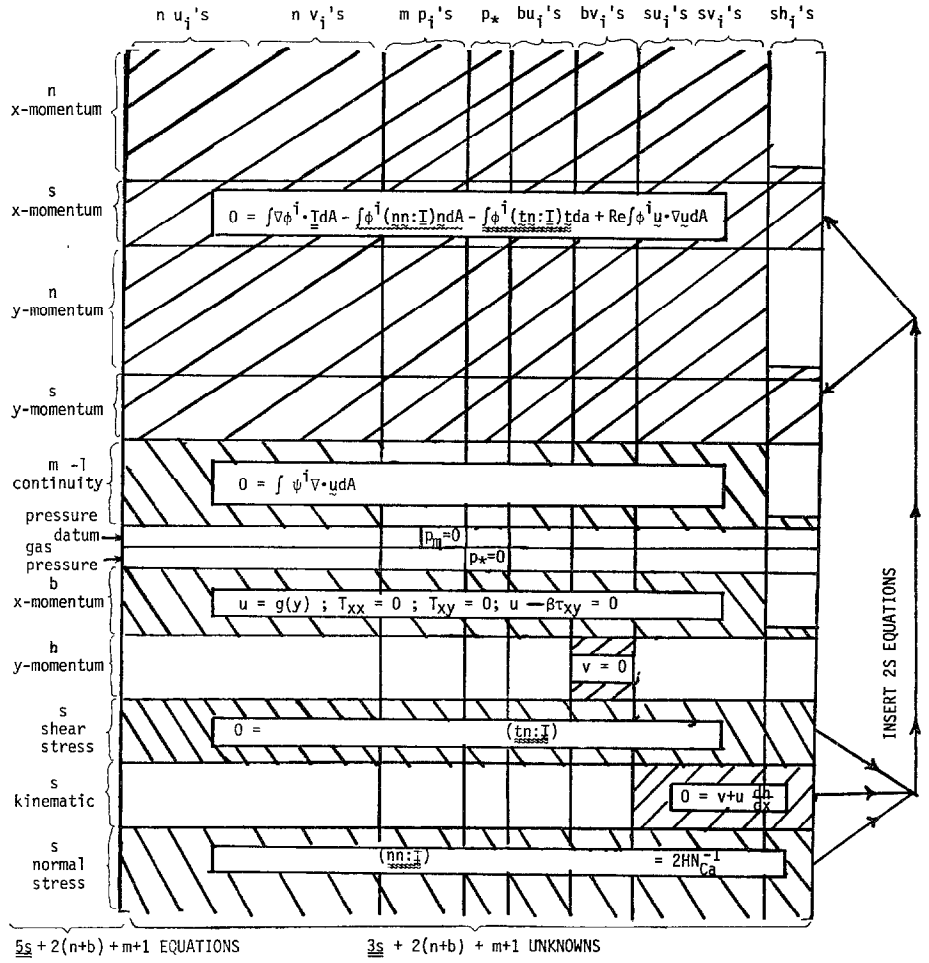

FIG. 2. Incidence array for free meniscus problem. n = number of internal velocity nodes; s = number of free meniscus velocity nodes; m = number of pressure nodes; b = number of velocity nodes on the part of the boundary excluding the free meniscus.

conditions on the velocity field (replacing s momentum equations), and retain the s normal stress boundary conditions as autonomous. There are yet other alternatives, including the use of linear combinations of equations (which could have advantages, as touched on below), but these are the most obvious because each eliminates one condition on the tangential component of a boundary vector and one condition on the normal component of a boundary vector. These two alternatives are evaluated in the next section.

In either case a nonlinear equation set must be solved. Although it could be solved all at once by standard nonlinear techniques, this approach has not appeared in the literature, evidently because the nodal elevations h_i occur as limits of residual integrals

(which need not be a hindrance, according to a study still in progress). Instead, the equation set has been partitioned into one subset of s meniscus equations and a second subset of the other $2s + 2(n + b) + m + 1$ equations. By fixing the s meniscus nodal elevations h_i, a flow field is calculated from the second subset; new h_i are then calculated from the first subset, and the process is repeated—the Picard iteration technique outlined in the Introduction. Basically it is a block Gauss–Seidel scheme [32] extended to nonlinear systems. Let the flow field unknowns be lumped together,

$$\mathbf{x}_i \equiv [\mathbf{u}_i, \mathbf{v}_i, \mathbf{p}_i]^{\mathrm{T}}. \tag{2.7}$$

Then schematically,

$$\mathbf{x}_i^{(n+1,m+1)} = [\mathbf{M}(\mathbf{x}_i^{(n+1,m)}, \mathbf{h}_i^{(n,l_c)})]^{-1} \times [\mathbf{b}_1(\mathbf{x}_i^{(n+1,m)}, \mathbf{h}_i^{(n,l_c)}) - \mathbf{S}_1(\mathbf{x}_i^{(n+1,m)}, \mathbf{h}_i^{(n,l_c)})\, \mathbf{h}_i^{(n,l_c)}], \tag{2.8}$$

$$\mathbf{h}_i^{(n+1,l+1)} = [\mathbf{B}(\mathbf{x}_i^{(n+1,m_c)}, \mathbf{h}_i^{(n+1,l)})]^{-1} \times [\mathbf{b}_2(\mathbf{x}_i^{(n+1,m_c)}, \mathbf{h}_i^{(n+1,l)}) - \mathbf{S}_2(\mathbf{x}_i^{(n+1,m_c)}, \mathbf{h}_i^{(n+1,l)})\, \mathbf{h}_i^{(n+1,l)}]. \tag{2.9}$$

Equation (2.8) represents the calculation of the flow field variables given a free surface location, $\mathbf{h}_i^{(n,l_c)}$. The first superscript on $\mathbf{x}_i$ indicates the $(n + 1)$ st flow field. A nonlinear system of equations must be solved to find the new $\mathbf{x}_i$ and the second superscript denotes this iteration: to start this iteration $x_i^{(n+1,0)} \equiv x_i^{(n,m_c)}$, where m_c denotes the converged solution at the nth level. $\mathbf{M}$ and $\mathbf{S}_1$ represent the linearized dependence of the momentum and continuity equations on $\mathbf{x}_i$ and $\mathbf{h}_i$, respectively, their forms depending on the type of iteration. $\mathbf{b}_1$ represents the forcing terms in the iteration and includes the residuals in a Newton scheme. Equation (2.9) represents the calculation of a new free surface location. The converged flow field from (2.8), given by $\mathbf{x}_i^{(n+1,m_c)}$, is used in this calculation and again a nonlinear iteration is necessary. $\mathbf{B}$ and $\mathbf{S}_2$ represent the linearized dependence of the boundary equations on $\mathbf{h}_i$ and $\mathbf{x}_i$, respectively; $\mathbf{b}_2$ is the forcing term. The iteration starts with $\mathbf{h}_i^{(n+1,0)} \equiv \mathbf{h}_i^{(n,l_c)}$, where l_c denotes convergence at the nth level. From now on we will drop the second superscript and leave it implicit whenever nonlinear systems are involved.

3. Free Meniscus Determination

3.1. *Kinematic Iteration*

Kinematic iteration means that after a flow field has been calculated a new free surface is determined from the kinematic condition. In differential form it is

$$\frac{dh^{(n+1)}}{dx} = \frac{v^{(n-1}}{u^{(n+1)}}. \tag{3.1}$$

For die swell, the boundary condition is $h^{(n+1)} = 1$ at $x = 0$. This and (3.1) can be discretized and linearized to give

$$
\begin{aligned}
h_1^{(n+1)} &= 1, \\
-h_1^{(n+1)} + h_2^{(n+1)} &= \int_{x_1}^{x_2} v^{(n+1)}(x, h^{(n)})/u^{(n+1)}(x, h^{(n)})\, dx \\
- h_2^{(n+1)} + h_3^{(n+1)} &= \int_{x_2}^{x_3} v^{(n+1)}(x, h^{(n)})/u^{(n+1)}(x, h^{(n)})\, dx \\
&\vdots \qquad\qquad\qquad \vdots \\
- h_{S-1}^{(n+1)} + h_S^{(n+1)} &= \int_{x_{S-1}}^{x_S} v^{(n+1)}(x, h^{(n)})/u^{(n+1)}(x, h^{(n)})\, dx.
\end{aligned} \tag{3.2}
$$

Here h_i is the meniscus height at node i which has x-coordinate x_i. The integrals are easily evaluated except for the first one. At the separation point x_1, both $v^{(n+1)}(x, h^{(n)})$ and $u^{(n+1)}(x, h^{(n)})$ are zero and their ratio is indeterminate from the finite element expansions. The difficulty can be sidestepped by employing an open-ended integration formula, for instance, Gaussian quadrature. Alternatively, integrating the continuity equation in the y-direction and invoking Eqs. (3.1) and (2.5f) generates an integral analog of (3.1):

$$
\int_0^{h_i} u(x_i, y)\, dy = \text{constant flow rate} \equiv Q. \tag{3.3}
$$

If a t-point Gaussian integration formula is employed in integrating (3.3) and on (0, 1) ξ_j is the jth Gauss point, with weighting w_j, then the discretized form is

$$
\begin{aligned}
\sum_{j=1}^{t} w_j u^{(n+1)}(x_1, \xi_j h_1^{(n+1)})\, h_1^{(n+1)} &= Q, \\
&\vdots \qquad\qquad\qquad \vdots \\
\sum_{j=1}^{t} w_j u^{(n+1)}(x_S, \xi_j h_S^{(n+1)})\, h_S^{(n+1)} &= Q.
\end{aligned} \tag{3.4}
$$

Because the ratio of velocities is not needed, this equation set also avoids the indeterminacy in the kinematic boundary condition at the separation point x_i; however, it is a nonlinear set of equations that must be solved instead of a linear set. The non-

TABLE I

Comparison of Various Iteration Schemes

	Time[a] per iteration		Total time[a] per iteration
	Free surface part	Flow part	
Kinematic iteration			
Differential	2×10^{-2}	8.6	8.6
Integral	1.5×10^{-1}	8.6	8.8
Normal stress	3×10^{-1}	8.6	8.9

[a] Time is in CPU seconds.

linear set proved to be many times more costly than the linear set (see Table I) and gave answers to within 1% of those of the differential form. The differential form originally proposed by Nickell *et al.* [18], thus is more effective in this application.

It is useful to represent the nonlinear equation set by an array *related* to the linearizations of it, the form of a linearization depending on the choice of iteration procedure (Newton, Picard iteration, etc.):

$$\left\{\begin{array}{c|c} \int_A \nabla\phi^i \cdot \mathbf{T}\, dA + N_{\mathrm{Re}} \int_A \phi^i \mathbf{u} \cdot \nabla \mathbf{u}\, dA & \begin{array}{c} \int_{\partial A} \phi^i\, 2H \frac{1}{N_{\mathrm{Ca}}}\, ds \\ \left(N_{\mathrm{Re}} \int_A \phi^i \mathbf{u} \cdot \nabla \mathbf{u}\, dA\right) \\ \left(\int_A \nabla\phi^i \cdot \mathbf{T}\, dA\right) \end{array} \\ \begin{array}{c} \int_A \psi^i \nabla \cdot \mathbf{u}\, dA \\ \text{Boundary Terms} \end{array} & \left(\int_A \psi^i \nabla \cdot \mathbf{u}\, dA\right) \\ \hline -v + u\frac{dh}{dx} & u\frac{dh}{dx} \end{array}\right\} = \left\{\begin{array}{c} \mathbf{b}_1 \\ \\ \\ \\ \hline \mathbf{b}_2 \end{array}\right\}. \tag{3.5}$$

The broken lines partitioning this incidence array separate terms in each equation which are the sources of corresponding elements in linearizing: in particular in the vertical column on the right, elements representing coefficients of h_i's; and in the horizontal column at the bottom, elements representing coefficients in the linearized free meniscus equations. The terms in parentheses represent quantities generated by coupling between flow field unknowns and free surface unknowns when the latter enter through the limits of integration. It turns out that the sum of squares of these terms is smaller than that of other terms in the same equations, reflecting a low degree of coupling with the interior of the flow field. If a Newton method is employed, the $\mathbf{b}_1$ and $\mathbf{b}_2$ terms also depend on flow field and free surface unknowns.

In the flow calculation an estimate of the mean curvature H must be made for each element along the meniscus. The isoparametric representation of the free surface, a quadratic function, could be used. However, the quadratic function cannot model even the gross behavior of the die-swell meniscus, because it requires increasing curvature as inclination falls, whereas in actuality *both* the curvature and slope of the meniscus *decrease* in the downstream direction. For this reason, the three nodal values of the free surface are fit to a circle and this is used to estimate the curvature. This approach is essentially the same as the one employed by Tanner [33] for a circular jet.

3.2. *Normal Stress Iteration*

The alternative is to use the normal stress conditions to calculate new meniscus locations $h_i^{(n+1)}$ after the $(n+1)$st approximation to the flow field has been calculated, the kinematic conditions having been satisfied as essential conditions in that calcula-

tion. This is basically the approach taken by Orr and Scriven [28], although they handled the kinematic conditions in a different way than is done here.

New profiles are generated from the discretized form of

$$\frac{d}{dx}\left\{\frac{h_x^{(n+1)}}{[1+(h_x^{(n+1)2}]^{1/2}}\right\} = N_{\mathrm{Ca}}\mathbf{n}^{(n+1)}\mathbf{n}^{(n+1)} : \mathbf{T}^{(n+1)}. \tag{3.6}$$

The boundary conditions on (3.6) for the die-swell case are

$$h(0) = 1; \tag{3.7}$$

$$h_x(L) = 0. \tag{3.8}$$

It appears inconsistent that the meniscus should have two boundary conditions in the normal stress iteration yet only one in the kinematic iteration. However, requiring in the kinematic case that $v = 0$ at $x = L$ in the flow field calculation ensures that (3.8) is satisfied if (3.1) is. Equation (3.6) is discretized by expanding h in a finite element basis and generating the Galerkin equations (cf. Orr *et al.* [34]). For the reasons given in Section 3.1, cubic basis functions were employed in the calculations and the resulting profiles interpolated to give the s nodal values of h_i needed in the isoparametric representation of the free surface. In the normal stress iteration scheme, a nonlinear equation set must be solved to get $h^{(n+1)}$. When Newton's method is used, convergence is rapid and CPU times per iteration are competitive with the linear iteration scheme presented in Section 3.1, as summarized by Table I.

The incidence array for this scheme is:

$$\left\{\begin{array}{c|c} N_{\mathrm{Re}}\int_A \phi^i\mathbf{u}\cdot\nabla\mathbf{u}\,dA & \left(N_{\mathrm{Re}}\int \phi^i\mathbf{u}\cdot\nabla\mathbf{u}\,dA\right) \\ +\int_A \nabla\phi^i\cdot\mathbf{T}\,dA - \int_{\partial A}\phi^i(\mathbf{nn}:\mathbf{T})\,\mathbf{n}\,ds & \left(\int \nabla\phi^i\cdot\mathbf{T}\,dA\right) \\ & \int_{\partial A}\phi^i(\mathbf{nn}\cdot\mathbf{T})\,\mathbf{n}\,ds \\ \int_A \psi^i\nabla\cdot\mathbf{u}\,dA & \left(\int_A \psi^i\nabla\cdot\mathbf{u}\,dA\right) \\ -v + u\dfrac{dh}{dx} & u\dfrac{dh}{dx} \\ \text{Boundary terms} & \\ \hline \int \rho^i(x)\,N_{\mathrm{Ca}}\mathbf{nn}:\mathbf{T}\,dx & \int \rho^i(x)\,2H\,dx \\ & +\int \rho^i(x)\,N_{\mathrm{Ca}}\mathbf{nn}:\mathbf{T}\,dx \end{array}\right\} = \left\{\begin{array}{c} \mathbf{b}_1 \\ \\ \\ \\ \\ \\ \hline \mathbf{b}_2 \end{array}\right\}. \tag{3.9}$$

The structure of the array is the same as that of (3.5) but the entries are different. $\rho^i(x)$ are the free surface basis functions in the Galerkin expansion of $h(x)$.

Equations (3.5) and (3.9) make apparent the interdependence of flow field and meniscus. In both incidence arrays, the upper right portion contains entries that put free surface unknowns into flow field equations. The degree of coupling depends on the relative magnitude of the terms involving these unknowns and obviously is controlled by the capillary number, N_{Ca}. Similarly, the lower left portion contains entries that put flow field unknowns into the free surface equations reflecting the sensitivity of meniscus shape to the underlying fluid motion. While the structure is the same for both iteration schemes, the rate of convergence is likely to depend on which scheme is chosen and on the magnitude of N_{Ca}.

3.3. *Convergence Tests*

Calculations were programmed for the CDC CYBER 74 at the University of Minnesota. Unknowns were numbered by columns in the y-direction (see Fig. 1) and the matrices stored in band form. The flow field matrices required the largest storage and for an 11 × 4 mesh the matrix size is 386 × 81. Matrices were inverted with a space-preserving, unsymmetric band solver [35]. Core requirements approached the limit of available storage, 150,000 64-bit octal words.

The two iteration procedures just described are implemented with (2.8) and (2.9). Given a meniscus location, (2.8) is solved to generate a flow field; this flow field is then substituted into (2.9) to update the estimate of the meniscus shape. Except in the

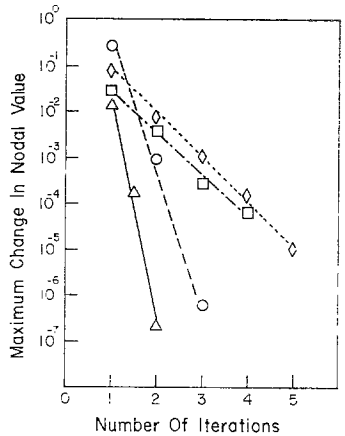

FIG. 3. Convergence of iterative schemes: ——, solution of normal stress boundary condition for a free surface by Newton's method; – – –, solution of momentum and continuity equations via Newton's method; — · —, overall iteration for free surface via normal stress iteration scheme: successive approximations; - - -, overall iteration for free surface via kinematic iteration scheme: successive approximations.

creeping flow limit ($N_{Re} = 0$), (2.8) is nonlinear. When Newton's method is employed to solve it, second-order convergence is achieved, as shown in Fig. 3. Iteration is continued until the maximum change in nodal values of velocity and pressure falls below 10^{-4}. When the normal stress iteration scheme is employed, (2.9) is also nonlinear. It too is solved by Newton's method, which again gives second-order convergence (Fig. 3); iteration is continued until the maximum change in meniscus nodal heights is less than 10^{-4}. While flow field and normal stress calculations exhibit second-order convergence, the overall iteration for **x** and **h** given by (2.8) and (2.9) is a Picard iteration scheme which, as is normal, becomes first order when it succeeds. See Fig. 3.

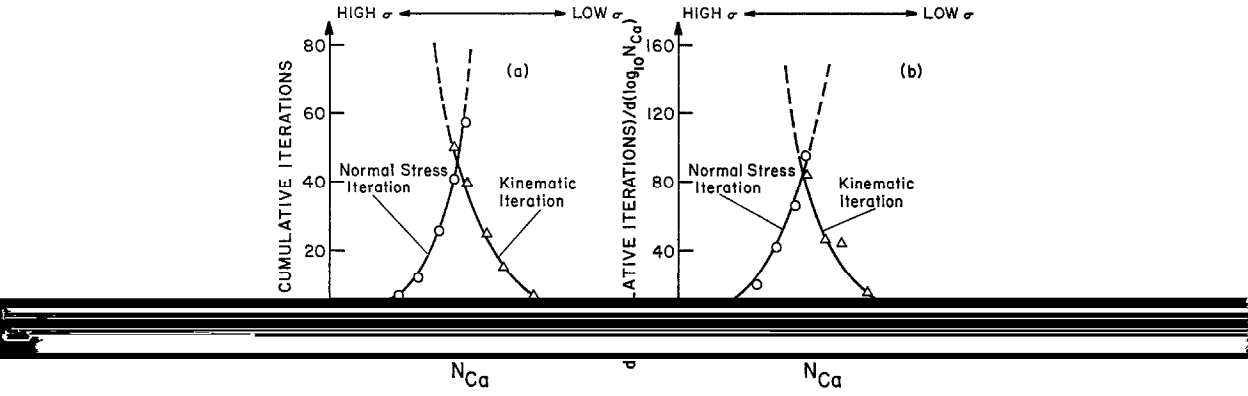

FIG. 4. Comparison of two iteration schemes: (a) number of iterations vs N_{Ca} ; (b) incremental iterations needed for a unit increase in N_{Ca} .

The ranges of convergence of the two iteration schemes are shown in Fig. 4a. At low capillary numbers the normal stress scheme converges whereas the kinematic scheme does not, and conversely at high capillary numbers. At intermediate capillary numbers there is a range of overlap where both schemes succeed but both are slow to converge. To achieve convergence for $N_{Ca} > 2/3$ for the normal stress scheme and for $N_{Ca} < 1$ for the kinematic scheme, underrelaxation proved necessary. The rate of convergence in both at capillary numbers near one was less than first order. Because the time per iteration in each scheme is nearly the same (Table I), the one taking the fewer iterations is the one to choose in the overlap range. In both schemes, solutions were generated by raising or lowering $\log_{10} N_{Ca}$ by a small amount and using the previous solution as an initial guess. The incremental work needed to get convergence for a unit change in $\log_{10} N_{Ca}$ is given in Fig. 4b; it is determined by numerically differentiating Fig. 4a.

The convergence properties of these two schemes can be understood by studying the linearized problem generated by setting constant the matrices and vectors in (2.8) and (2.9) and scaling the two parts with N_1 and N_2 chosen according to the

magnitude of $\mathbf{S}_1$ relative to $\mathbf{M}$ and of $\mathbf{S}_2$ relative to $\mathbf{B}$. The iteration procedure becomes

$$\mathbf{x}^{(n+1)} = \mathbf{M}^{-1}[\mathbf{b}_1 - N_1\mathbf{S}_1\mathbf{h}^{(n)}], \tag{3.10}$$

$$\begin{aligned}\mathbf{h}^{(n+1)} &= \mathbf{B}^{-1}[\mathbf{b}_2 - N_2\mathbf{S}_2[\mathbf{M}^{-1}[\mathbf{b}_1 - N_1\mathbf{S}_1\mathbf{h}_1^{(n)}]]] \\ &= \mathbf{B}^{-1}\mathbf{b}_2 - N_2\mathbf{B}^{-1}\mathbf{S}_2\mathbf{M}^{-1}\mathbf{b}_1 + N_1N_2\mathbf{B}^{-1}\mathbf{S}_2\mathbf{M}^{-1}\mathbf{S}_1\mathbf{h}_1^{(n)}.\end{aligned} \tag{3.11}$$

These are simplified by defining

$$\mathbf{\Lambda} \equiv \mathbf{B}^{-1}\mathbf{b}_2 - N_2\mathbf{B}^{-1}\mathbf{S}_2\mathbf{M}^{-1}\mathbf{b}_1\,, \tag{3.12}$$

$$\mathbf{X} \equiv N_1N_2\mathbf{B}^{-1}\mathbf{S}_2\mathbf{M}^{-1}\mathbf{S}_1\,, \tag{3.13}$$

which lead to the following formulas for the iteration:

$$\mathbf{h}^{(n)} = (\mathbf{1} + \mathbf{X} + \mathbf{X}^2 + \cdots + \mathbf{X}^{n-1})\,\mathbf{\Lambda} + \mathbf{X}^n\mathbf{h}^{(0)}, \tag{3.14}$$

$$\mathbf{x}^{(n+1)} = \mathbf{M}^{-1}\mathbf{b}_1 - N_1\mathbf{M}^{-1}\mathbf{S}_1\mathbf{h}^{(n)}. \tag{3.15}$$

Here $\mathbf{h}^{(0)}$ is the initial estimate of the meniscus profile. The iteration obviously converges provided $\mathbf{h}^{(n)}$ converges as $n \to \infty$.

The criterion of convergence can be expressed in terms of the matrix $\mathbf{X}$, viz.,

$$[\mathrm{tr}(\mathbf{X} * \mathbf{X}^{\mathrm{T}})]^{1/2} < \tfrac{1}{2}. \tag{3.16}$$

From (3.13) it is plain that if the product N_1N_2 is sufficiently small, the iteration converges; i.e., provided the magnitudes of $\mathbf{S}_1$ and $\mathbf{S}_2$, the rectangular matrices that stem from the upper right and lower left portions of the incidence arrays (3.5) and (3.9), are small (in the sense of the norm in (3.16)) compared to $\mathbf{M}$ and $\mathbf{B}$ the iteration converges. Moreover, convergence depends only on the product of N_1 and N_2. So, provided either measure of the coupling of flow field and meniscus shape is sufficiently small, convergence is attained.

The iterations represented by (3.5) and (3.9) take the form of (3.10) and (3.11) but have the added complication of nonlinearity. Under conditions in which the corresponding linearized problem diverges the nonlinear problem does so also. In the kinematic iteration represented by (3.5), the magnitude of N_1 is controlled by the ratio of normal viscous stress to capillary pressure at the meniscus, i.e., the size of N_{Ca}. If in the momentum equations viscous stress contributions dominate those of capillary pressure, the nonlinear iteration scheme converges; but when N_{Ca} becomes very small and capillarity dominates, the nonlinear scheme diverges. By contrast, in the normal stress iteration represented by (3.9), N_2 is governed by the magnitude of the capillary number. Provided capillary terms dominate the normal stress boundary condition, convergence is attained; however, as N_{Ca} increases and viscous normal stresses take over, N_2 grows and the iteration diverges.

4. Results

At low Reynolds numbers the liquid sheet issuing from the sharp-cornered slot exhibits the phenomenon known as die swell, which is portrayed in Fig. 1. If the effect of gravity is insensible the sheet of Newtonian liquid reaches a final thickness approximately 20% greater than the slot breadth, according to the finite-element calculation of Patton and Finlayson [36] for vanishingly small Reynolds number, no surface tension, and no slip on the channel walls. This solution is confirmed by earlier results of the present investigation [11]. In the laboratory much more pronounced die swell is often seen in non-Newtonian flow; yet at such low shear rates that the same fluid behaves in the Newtonian manner, swell ratios of approximately 1.2 have been measured [37].

TABLE II

Wall Shear Stress at Exit and Integrated Wall Stress for No-Slip and Slip ($B = 10^{-2}$) Cases

Size of smallest element (mesh)[a] ($\times$ half-width)		Shear stress in die swell	
		Stress ($x = 0-$)	Shear force ($= \int_{-2}^{0} \tau_w \, dx$)
		No slip	
0.08	(9×3)	7.9	6.5
0.08a	(9×3)	8.1	6.6
0.08b	(10×4)	8.3	6.5
0.08	(11×4)	8.1	6.5
0.08	(11×4)	8.1	6.5
0.06c	(13×4)	8.4	6.5
0.04	(12×4)	12.2	6.6
		Slip ($B = 10^{-2}$)	
0.08a	(9×3)	5.8	6.4
0.08b	(10×4)	5.8	6.4
0.08	(11×4)	5.8	6.4
0.06c	(13×4)	5.7	6.4

[a] a, b, c indicate identical meshes.

4.1. *Flow with No Slip at Channel Wall*

As the finite-element mesh is refined in the vicinity of the contact/separation line, our no-slip solutions show ever-increasing stress in the neighborhood of the line and thus provide strong evidence of a singularity at the line: compare Table II and the shear stress distribution plotted for reference in Fig. 5. These creeping flow ($N_{\mathrm{Re}} = 0$) results accord with the expectation that shear stress on the wall in the vicinity of the contact line follows the relation

$$\tau_{xy} \propto (-x)^{-1/2}, \qquad x < 0,$$

i.e., the expectation that the singularity is integrable to a finite shear force on any finite length of wall, as indicated by the model analysis of Michael [7] and the numerical computations of circular die swell by Nickell *et al.* [18].

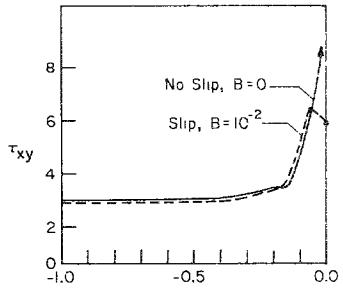

FIG. 5. Upstream wall shear stress profile $N_{Re} = 0$, $N_{Ca} = \infty$.

Three-dimensional visualizations of the velocity, pressure, and subsidiary fields provide insight into the nature of the flow. The field of the main velocity component in Fig. 6a indicates the velocity rearrangement from parabolic to plug flow. Evident are velocity inflections, which may presage instability. The rearrangement is restricted to a small region near the exit plane and clearly the application of the inlet and outlet boundary conditions two or more half-diameters from the exit is a reasonable approximation. The field of the transverse velocity component is drawn to the same scale in Fig. 6b. It of course is much smaller, asymmetric, and significant only in the regions where rearrangement is occurring. The pressure falls linearly along the die, where it is driving a Poiseuille flow, and far downstream in the liquid sheet it reaches zero. The pressure plot in Fig. 6c (note that the negative of the pressure is plotted) indicates a singularity at the separation lines, which raises the possibility of cavitation at the exit. However, the physics of cavitation in intense, anisotropic viscous stress fields is unknown (failure partly in shear is a possibility not unrelated to the slip issue). The difference between the normal viscous stresses in the streamwise, τ_{tt}, and transverse, τ_{nn}, directions is shown in Fig. 6d. The plot reveals that even in Newtonian liquid, large normal stress differences can be generated near the exit plane. We assess the oscillations near the wall at the exit to be of numerical origin and to result from the representation of the solution by a finite rather than infinite basis. The solution satisfies both the continuity requirement, which dictates that the normal stress difference along the wall is zero ($\partial u/\partial x = 0$ since there is no slip and hence $\partial v/\partial y = 0$), and the normal stress condition along the interface.

The latter dictates that on the interface the viscous normal stress, τ_{nn}, must balance the normal pressure force and the capillary pressure force of the meniscus. At the exit the latter appears to remain bounded and thus if the normal pressure force is singular there, so must also be both the viscous normal stress and the normal stress difference, because $\tau_{tt} - \tau_{nn} = -2\tau_{nn}$. In the finite element solution the response to

the discontinuity in boundary condition is not a discontinuous normal stress difference but rather one that oscillates within a neighborhood of the exit which shrinks as the mesh is refined near the exit. Figure 6e, the vorticity distribution, demonstrates the continual diffusive flux of vorticity across the flow field, as much entering at one wall as leaves at the other. In the free liquid sheet, as much is generated by flow along the one curved meniscus as is consumed at the other. Symmetry also makes the *net* vorticity zero in each cross section. Far downstream the meniscus becomes flat and the vorticity level ultimately reaches zero everywhere in the flow.

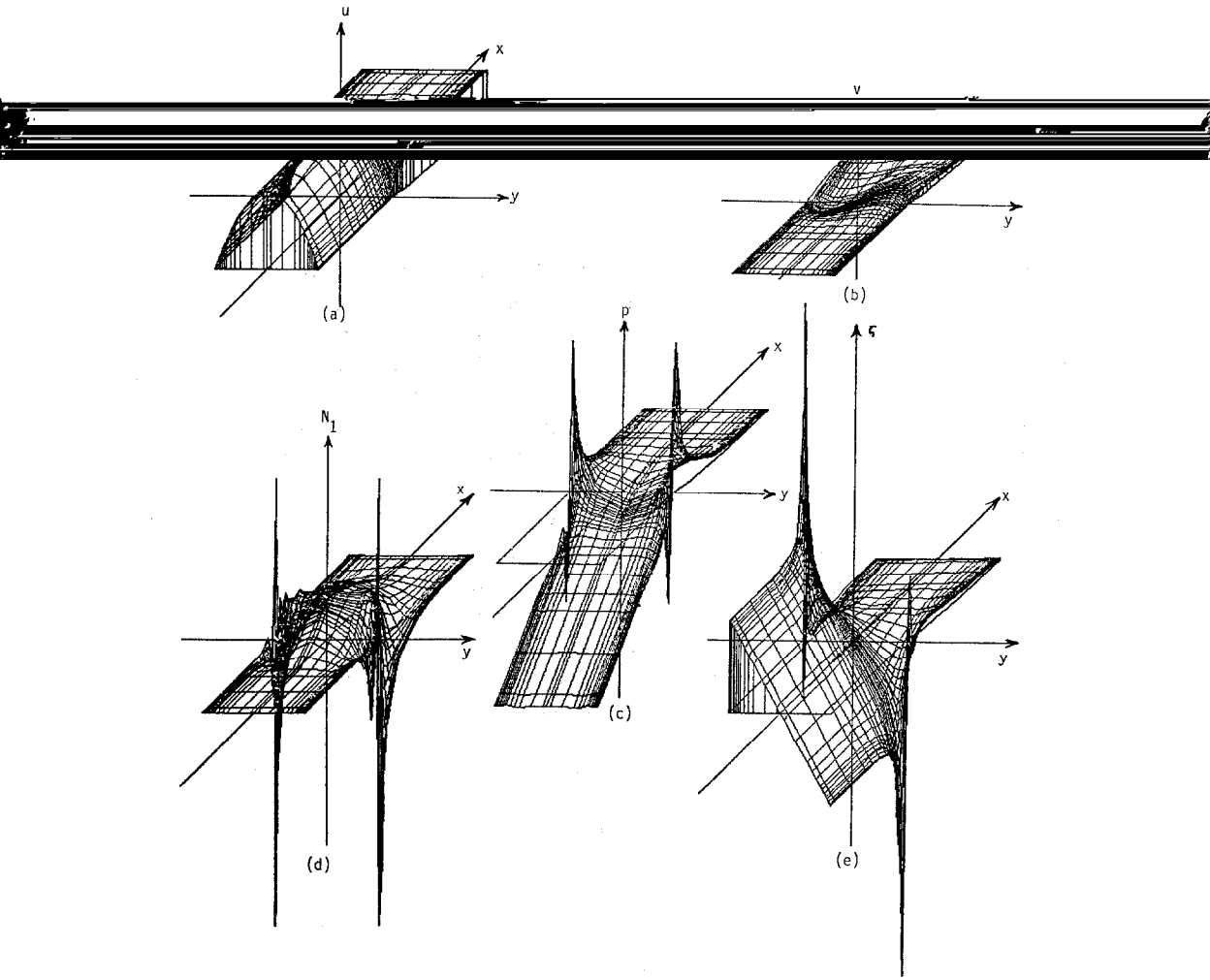

FIG. 6. Three-dimensional visualization of flow field: Re = 0, $N_{Ca} = \infty$, $B = 0$. (a) u-velocity field; (b) v-velocity field; (c) pressure: scaled by -0.4; (d) $N_1 \equiv T_{ss} - T_{nn}$, streamwise minus perpendicular normal stress, scaled by -0.4; (e) vorticity, $\zeta = u_y - v_x$, scaled by 0.6.

4.2. *Effect of Slip Coefficient Boundary Condition*

Results for values of the slip parameter, B, from 0 to 1 in creeping flow are plotted in Figs. 5, 7, and 9. Shear stress on the wall upstream of the contact line when $B = 0.01$ is compared with the no-slip distribution in Fig. 5. Results of mesh refinement are summarized in Table II; they strongly indicate that the apparent singularity in the no-slip solution is removed by adopting Navier's slip hypothesis rather than the no-slip postulate. Evidently any value of the slip coefficient β in (1.1) greater than zero suffices. This raises the question of the sensitivities of the various locales and aspects of the flow field to the magnitude of β, or of the dimensionless slip parameter B.

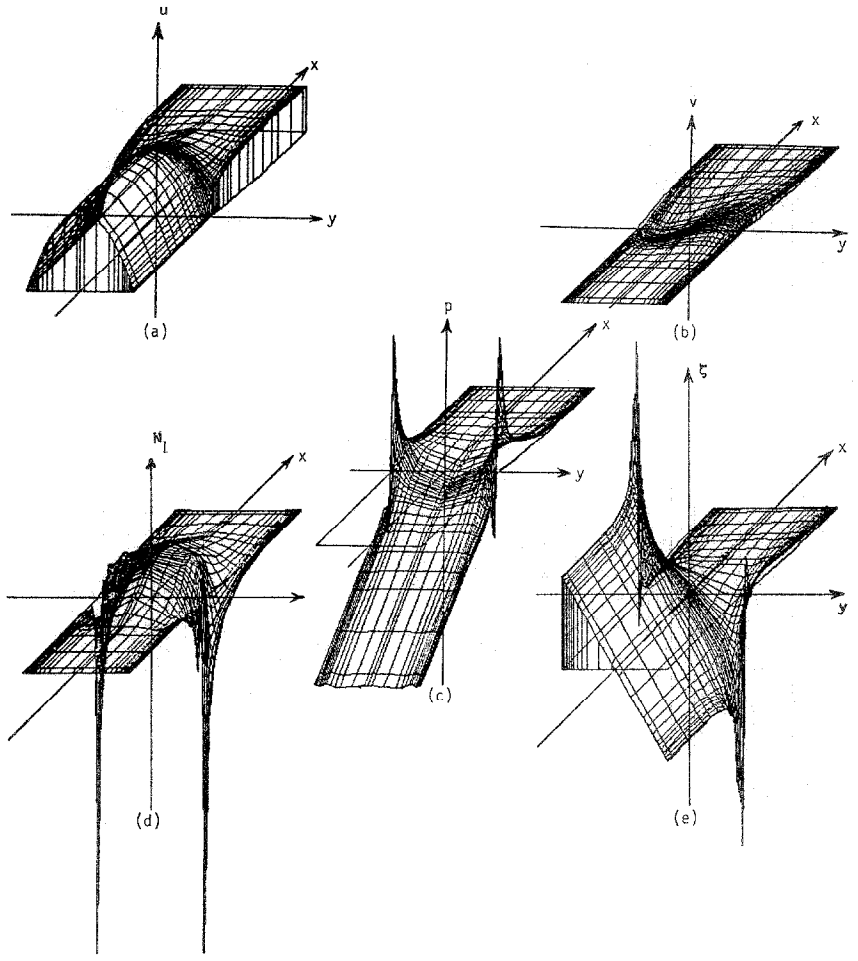

FIG. 7. Three-dimensional visualization of flow field: Re = 0, $N_{Ca} = \infty$, $B = 10^{-2}$. Same definitions and scaling as in Fig. 6.

There are three integral measure of the effect of slip: the die-swell ratio $h(L)/b$; the meniscus separation inclination, which is defined as the slope of a plane through the contact/separation line and the meniscus at a fixed distance downstream; and the extrapolation of upstream pressure on the wall to the channel exit. The effect of slip on these at $N_{Re} = 0$ is described elsewhere [11]. For reference, the die-swell ratios for creeping flow and vanishing surface tension are plotted in Fig. 9. When $B < 10^{-3}$, slip has no perceptible influence on die-swell ratio; nor does it influence meniscus separation inclination, or extrapolated pressure at the exit.

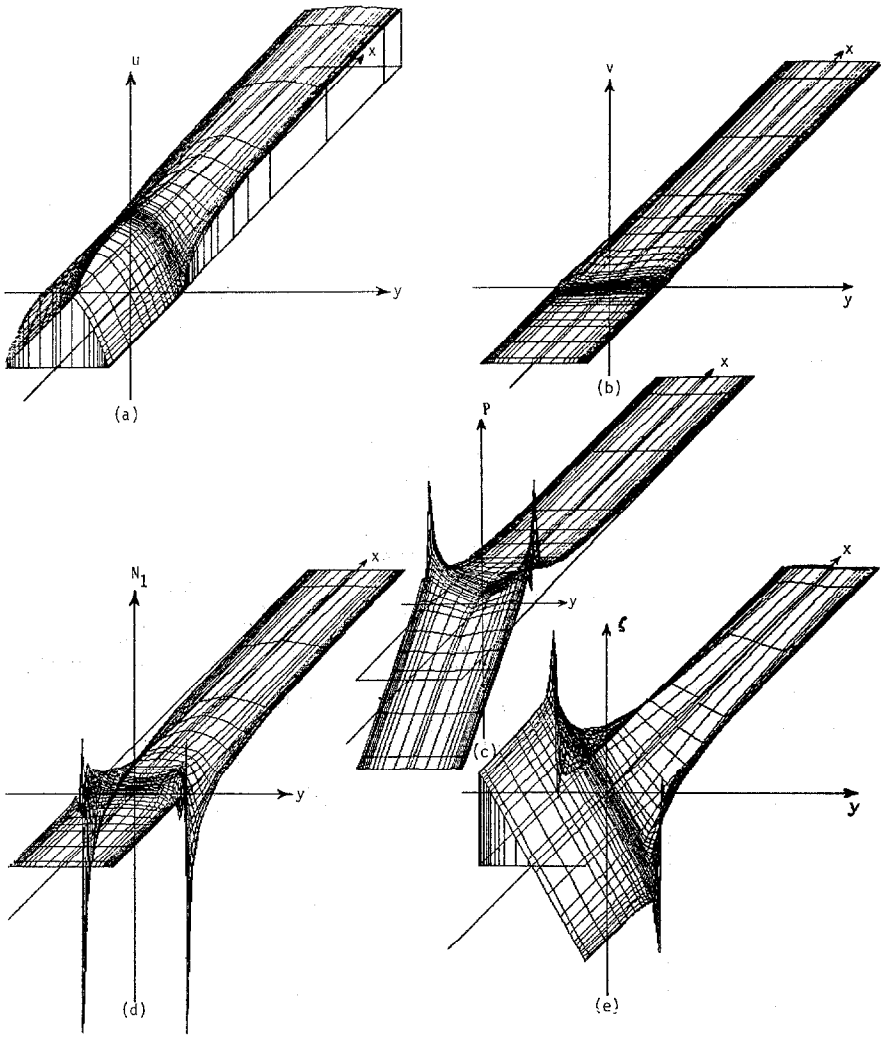

FIG. 8. Three-dimensional visualization of flow field: Re = 20, $N_{Ca} = \infty$, $B = 0$. Same definitions and scaling as in Fig. 6.

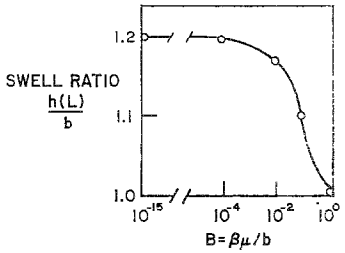

FIG. 9. Die swell as a function of slip parameter.

In contrast, when $B > 10^{-3}$ the die-swell ratio is significantly lowered. Slip reduces momentum transfer to the wall upstream of the slot exit. The liquid exits with higher momentum content and so evolves into a faster moving, thinner sheet downstream. The reduction in swell ratio with slip of a viscoelastic non-Newtonian liquid can be dramatic, as reported by Kraynik [38].

Our results point toward similar though much less pronounced swell reduction by slip of Newtonian liquid in the high shear region just upstream of the exit of a round channel.

Three-dimensional visualizations of the flow field when $B = 10^{-2}$ are given in Fig. 7. Although the x-velocity component still undergoes considerable rearrangement and an inflection point in the downstream region is still present, the die swell is clearly reduced. The pressure gradient is slightly less than that in the no-slip case and hence the pressure profile is flatter. The vorticity is no longer singular at the exit; moreover, it is lower in magnitude throughout the channel, for the velocity profile is flatter. There are corresponding reductions in the y-velocity profile and normal stress difference but the normal stress differences near the exit plane continue to be significant.

4.3. *Effect of Restricting Slip to Exit Region*

The slip coefficient boundary condition (1.1) generates appreciable velocity discontinuity only where the wall shear stress is high. The question arises as to whether restricting slip to the neighborhood upstream of the separation/contact line can effectively remove the stress singularity yet leave the velocity and pressure fields significantly less altered from those of the no-slip case. Calculations were made in which slip was allowed only within 0.18b of the exit. A uniform slip coefficient $B > 0$ was specified for $-0.18\text{b} < x < 0$ and $B = 0$ was specified for $x < -0.18\text{b}$. Either two or three elements were placed within this region. Comparison of the results proved that the solution is insensitive to the number of elements in this region. However, it was necessary to use a refined mesh further upstream than in cases of uniform slip. The reason is the added velocity rearrangement and concomitant increase in stress near the point of change in boundary condition, i.e., at $x = -0.18\text{b}$.

The effect of local slip on die swell is shown in Fig. 10. When $B < 10^{-2}$ within

viscous diffusion of momentum across the flow. With increasing Reynolds number the relaxing velocity profiles are shifted further downstream and thus the flow development length rises. This is clear in the three-dimensional visualization of flow at $N_{Re} = 20$ in Fig. 8. Whereas at $N_{Re} = 0$, the x-veloxity profile rearranges to within 1 % of the final value in approximately 1.5 half-widths, at $N_{Re} = 20$ this transition takes more than two half-widths.

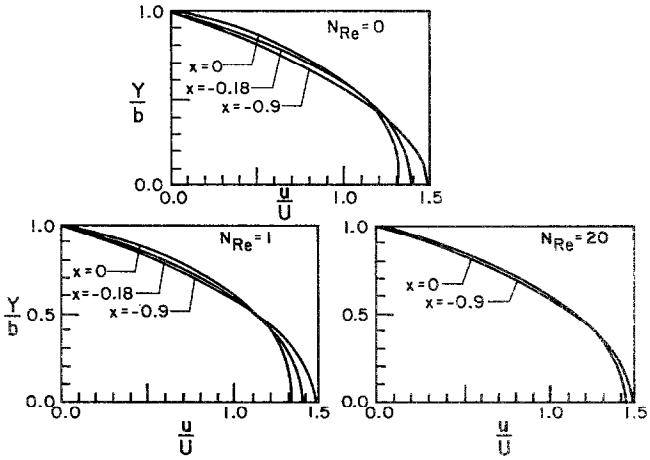

FIG. 11. Upstream influence on the velocity field and its reduction with increasing Reynolds number.

Because the upstream velocity field rearrangement is confined to a region near the exit the rapid pressure and vorticity variations are also confined to a small region as is evident in Fig. 8. The normal stress difference near the exit plane is much reduced at the higher Reynolds number.

4.5. *Effect of Surface Tension*

Uniform surface tension in the free meniscus can act only where the meniscus is curved. There it develops the capillary pressure difference $p - p_0 = 2H\sigma$ which, through the pressure field of which it is a part, can influence the entire flow. From another point of view the action of surface tension in the meniscus at the contact/separation line is to transmit to the solid a certain amount of momentum which the curved meniscus removes from the liquid downstream of the exit plane as the velocity distribution relaxes toward plug flow. The effect is to reduce the swell ratio.

The appropriate dimensionless parameter is the capillary number, which measures the ratio of viscous to surface tension forces. If surface tension were absent, the normal stress boundary condition would require the pressure difference across the free surface to be exactly compensated by the viscous normal stress on the liquid side. Surface tension enters and alters this balance increasingly as $N_{Ca} \equiv \mu U/\sigma$ is raised. In

Fig. 12, the straightening of the meniscus profile with rising surface tension is shown. The high tension calculations were made with the normal stress iteration scheme and the low tension ones with the kinematic iteration scheme. At $N_{Ca} = 2$ the meniscus was calculated with both schemes and the results were identical on the scale of Fig. 12. On a greatly increased scale, the differences of meniscus profiles from the two schemes are shown in Fig. 13. The discrepancy at all points along the meniscus is less than 1 %.

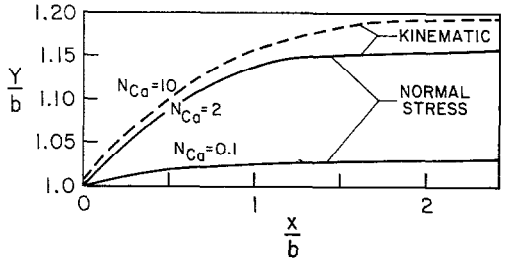

FIG. 12. Meniscus profile as a function of capillary number. – – –, kinematic iteration scheme; ——, normal stress iteration scheme.

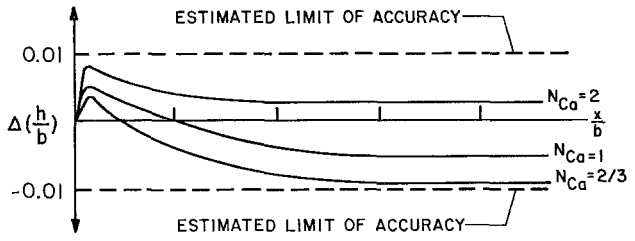

FIG. 13. Comparison of kinematic and normal stress iteration scheme solutions in overlap region. $N_{Re} = 0$, $B = 0$.

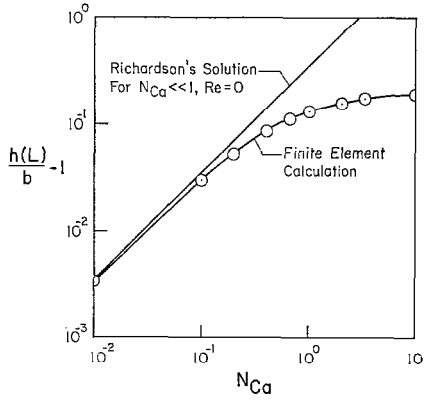

FIG. 14. Comparison of Richardson's [41] asymptotic results for swell ratio with finite element calculations.

These results can be compared with Richardson's [41] asymptotic prediction for vanishingly small Reynolds and capillary numbers. Richardson used the Wiener–Hopf technique to generate the perturbation solution shown in Fig. 14. That solution is seen to be accurate for $N_{Ca} < 0.1$ and to break down progressively as capillary number increases. Richardson's approach is similar to the first iteration in the normal stress scheme of Section 3.2; however, he used a *linearized* normal stress condition. In view of the convergence behavior of the normal stress iteration scheme (Section 3.3), it is not surprising that his approach leads to a good approximation only at low capillary numbers.

5. Concluding Remarks

The finite element technique has proved to be a valuable aid in gaining understanding of meniscus flows. However, more remains to be learned about optimizing the technique itself. A framework has been presented from which finite element free surface iteration schemes can be developed, and evaluated as to their likelihood of convergence. Two schemes have been investigated and it was found that surface tension discriminated between them. At low surface tension ($N_{Ca} > 1$), a scheme employing the kinematic condition for calculating free surface shapes converged rapidly while a scheme employing the normal stress boundary condition for calculating shapes did not. At high surface tension ($N_{Ca} < 1$) the opposite was true. For $N_{Ca} \approx 1$, both schemes converged but convergence was slow. It is conceivable that convergence in this intermediate range might be most rapid if a suitable weighted sum of the two schemes were used. Another possibility is a hybrid iteration scheme in which the normal stress condition (Section 3.2) is used to determine the free surface shape in regions where high meniscus curvature makes surface tension important; and the kinematic scheme (Section 3.1) is employed elsewhere. Both iteration schemes discussed here are based on successive approximations to the free meniscus shape and will exhibit linear convergence at best. It seems likely that a Newton scheme based on the entire equation set (velocity, pressure, *and* free meniscus location unknowns) would enhance convergence. Even here, options exist regarding the way the free surface boundary conditions, the momentum equations, and the continuity equations are combined.

The effect of replacing the usual no-slip boundary condition by a slip boundary condition on solid boundaries was investigated in the die-swell problem. It was found that even if slip is possible, the no-slip boundary condition is accurate for Newtonian die swell provided $\beta\mu/b < 10^{-3}$; however, slip at the wall alleviates the apparent stress singularity at the separation/contact line. When $\beta\mu/b \geq 10^{-3}$, slip reduces die swell even of Newtonian liquid and might produce yet larger effects for non-Newtonian liquid. Even allowing only for local slip near the contact line where the stresses are greatest is sufficient to reduce die swell provided $\beta\mu/b \geq 10^{-3}$.

Die swell is also affected by other momentum sources, notably inertial and surface tension forces. Our results show that increasing inertial effects by raising Reynolds number decreases the upstream influence of the die exit on the velocity field, hence

reducing the momentum transfer to the die wall and decreasing die swell. While *decreasing* upstream influence, increasing Reynolds number *increases* the downstream lenth needed to achieve plug flow. Surface tension stresses were shown to straighten the meniscus profile and hence reduce die swell. While the results of Section 4 were generated by considering each momentum source independently, of course they may act in concert. Figure 15 shows the compounding effect of surface tension and slip along the die wall acting together to decrease die swell. Hence the finite-element technique can handle, in an easy manner, the combination of more than one momentum source, and further study toward optimization of free meniscus calculations seems warranted.

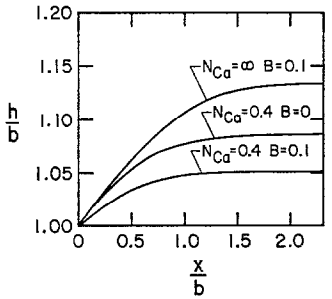

FIG. 15. Profile straightening compounded by the actions of surface tension and slip together.

ACKNOWLEDGMENTS

This research was supported by the National Science Foundation and the University of Minnesota Computing Center. W. J. Silliman held a Bush Foundation Fellowship. A summary of the paper was presented at the International Conference on Numerical Methods in Laminar and Turbulent Flow, University College of Swansea, July 1978.

REFERENCES

1. S. J. SALTER, Ph. D. thesis, University of Minnesota, Minneapolis, 1975.
2. M. C. DEL CERRO AND G. J. JAMESON, *J. Chem. Soc. Faraday Trans. 1* **72** (1976), 883.
3. S. J. SALTER, K. BENNETT, L. E. SCRIVEN, AND H. T. DAVIS, unpublished, 1978.
4. C. HUH, Ph. D. thesis, University of Minnesota, Minneapolis, 1969.
5. C. HUH AND L. E. SCRIVEN, *J. Colloid Interface Sci.* **35** (1971), 85.
6. S. RICHARDSON, *Proc. Cambridge Phil. Soc.* **67** (1970), 477.
7. D. H. MICHAEL, *Mathematika* **5** (1958), 1, 82.
8. L. M. HOCKING, *J. Fluid Mech.* **76** (1976), 801.
9. E. B. DUSSAN V., *J. Fluid Mech.* **77** (1976), 665.
10. C. HUH AND S. G. MASON, *J. Fluid Mech.* **81** (1977), 401.
11. W. J. SILLIMAN AND L. E. SCRIVEN, *Phys. Fluids* **21** (11) (1978), 2115.
12. G. D. TOWELL AND L. B. ROTHFELD, *AIChE J.* **12** (1966), 972.
13. J. KERN, *Verfahrenstechnik* **3** (1969), 425.

14. M. BENTWICH, D. GLASSER, J. KERN, AND D. WILLIAMS, *AIChE J.* **22** (1976), 772.
15. C. L. M. H. NAVIER, *Mem. Acad. R. Sci. Inst. Fr.* **6** (1827), 389.
16. G. G. STOKES, *Trans. Cambridge Phil. Soc.* **9** (1851), 8.
17. W. C. D. WHETHAM, *Phil. Trans. Roy. Soc. Ser. A* **181** (1890), 559.
18. R. E. NICKELL, R. I. TANNER, AND B. CASWELL, *J. Fluid Mech.* **65** (1974), 189.
19. L. M. HOCKING, *J. Fluid Mech.* **77** (1977), 209.
20. E. B. DUSSAN V. AND S. B. DAVIS, *J. Fluid Mech.* **65** (1974), 71.
21. S. RICHARDSON, *J. Fluid Mech.* **59** (1973), 707.
22. J. C. CHAUFFOUREAUX, C. DEHENNAU, AND J. VAN RIJCKEVORSEL, 70th Annual Meeting of AIChE, New York, 1977.
23. B. DERYAGUIN, G. STRAKHOVSKY, AND D. MALYSHEVA, *Acta Physicochim. URSS* **19** (1944), 541.
24. J. LYKLEMA, AND J. TH. G. OVERBEEK, *J. Colloid Sci.* **16** (1961), 501.
25. G. N. PATTERSON, "Molecular Flow of Gases," Wiley, New York, 1956.
26. C. TAYLER AND P. HOOD, *Comp. Fluids* **1** (1973), 73.
27. D. K. GARTLING, R. E. NICKELL, AND R. I. TANNER, *Int. J. Num. Meth. Eng.* **11** (1977), 1155.
28. F. M. ORR AND L. E. SCRIVEN, *J. Fluid Mech.* **84** (1978), 145.
29. B. G. HIGGINS, W. J. SILLIMAN, R. A. BROWN, AND L. E. SCRIVEN, *Ind. Eng. Chem. Fundam.* **16** (1977), 393.
30. G. STRANG AND G. J. FIX, "An Analysis of the Finite Element Method," Prentice-Hall, Englewood Cliffs, 1973.
31. M. A. STADTHERR, W. A. GIFFORD, AND L. E. SCRIVEN, *Chem. Eng. Sci.* **29** (1974), 1025.
32. G. E. FORSYTHE AND W. R. WASON, "Finite-Difference Method for Partial Differential Equations," Wiley, New York, 1960.
33. R. I. TANNER, "Proceedings, Seventh International Congress on Rheology," Gothenburg, Sweden 1965, p. 140.
34. F. M. ORR, L. E. SCRIVEN, AND A. P. RIVAS, *J. Colloid Interface Sci.* **52** (1975), 602.
35. M. FRISCH, "BANSOL," University Computer Center, University of Minnesota, 1976.
36. T. W. PATTON AND B. A. FINLAYSON, 70th Annual Meeting of AIChE., New York, 1977.
37. D. C. HUANG AND J. L. WHITE, "Polymer Science & Engineering Report No. 113," University of Tennessee, Knoxville, 1978.
38. A. KRAYNIK, Ph. D. thesis, Princeton University, 1977.
39. R. L. FOSDICK, personal communication, 1978.
40. D. B. HARMON, *J. Franklin Inst.* **259** (1955), 519.
41. S. RICHARDSON, *Rheol. Acta* **9** (1970), 193.